Volume 17
Number 10
11 March 2026
Pages 4831–5282

Chemical Science

rsc.li/chemical-science

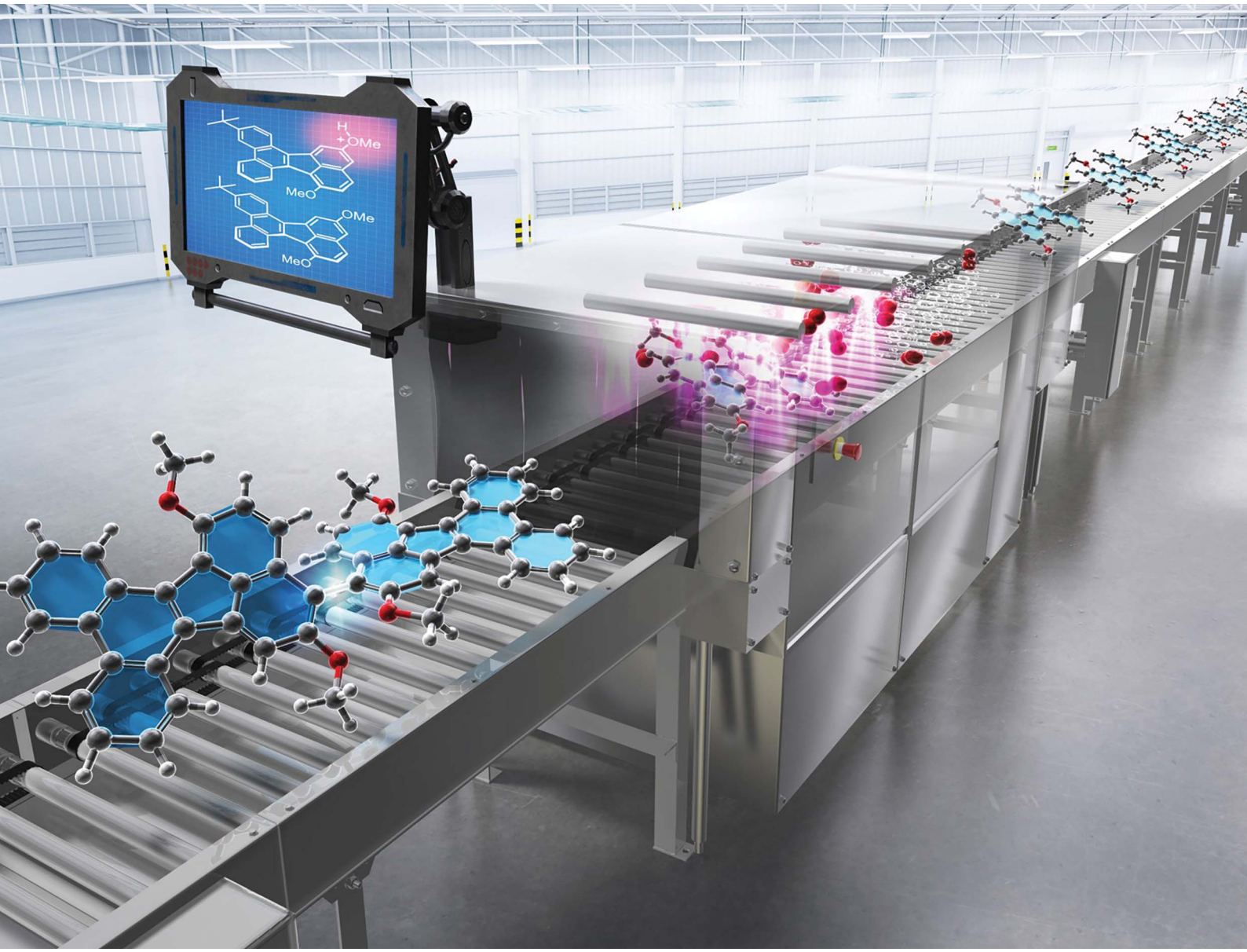

ISSN 2041-6539

ROYAL SOCIETY OF CHEMISTRY

EDGE ARTICLE

Kiyosei Takasu *et al.*

Self-induced charge transfer activation enables metal-free C–H coupling of polycyclic aromatic hydrocarbons under photo irradiation

Chemical Science

ROYAL SOCIETY OF CHEMISTRY

EDGE ARTICLE

View Article Online
View Journal | View Issue

Open Access Article. Published on 10 February 2026. Downloaded on 3/24/2026 4:28:19 PM.
This article is licensed under a Creative Commons Attribution-NonCommercial 3.0 Unported Licence.

Check for updates

Cite this: *Chem. Sci.*, 2026, **17**, 4942

All publication charges for this article have been paid for by the Royal Society of Chemistry

Self-induced charge transfer activation enables metal-free C–H coupling of polycyclic aromatic hydrocarbons under photo irradiation

Kazuma Kurokawa,[a] Aki Kohyama,[a] Yusuke Kuroda,[a] Keisuke Tao-Kakuyama,[b] Hiroshi Takikawa[a] and Kiyosei Takasu *[a]

Received 23rd November 2025
Accepted 6th February 2026

DOI: 10.1039/d5sc09144f

rsc.li/chemical-science

Axially chiral three-dimensional nanographenes (3D NGs) represent promising scaffolds for chiral optoelectronic materials, yet their direct synthesis remains challenging because of the oxidative fragility of π-extended arenes. Here we report a metal-free, photo-irradiated oxidative C–H/C–H biaryl coupling of polycyclic aromatic hydrocarbons mediated by a Brønsted acid and O_2. The reaction efficiently converts π-extended arenols, including fluoranthene derivatives, into structurally diverse axially chiral 3D NGs without overoxidation. Mechanistic studies reveal that self-induced charge transfer (CT) complexation between protonated and neutral arenols triggers photoinduced formation of radical cations, as supported by UV-vis, ESR and DFT analyses. The obtained axially chiral 3D NGs exhibit high configurational stability and photophysical features rationalized by TD-DFT calculations. This strategy establishes a general platform for constructing axially chiral 3D NGs from π-extended arenols under metal-free conditions.

Introduction

Nanographenes (NGs), atomically precise graphene fragments with tunable dimensionally, have emerged as ideal scaffolds for chiral optoelectronic systems.[1] In particular, three-dimensional (3D) NGs are attracting attention because their contoured, shape-persistent topologies mitigate π–π aggregation while amplifying chiroptical responses. Representative architectures based on triptycene-,[2,3] cyclooctatetraene-,[4–7] spirocyclic-,[8,9] and biaryl[10–15]-frameworks (Fig. 1a) exemplify this design principle. Among these, biaryl-type NGs are attractive for accessing axially chiral frameworks and serving as precursors to more complex 2D and 3D materials.[8,16,17] However, only a limited handful of synthetic examples have been reported (Fig. 1b). Because most reported routes rely on cross couplings of prefunctionalized substrates, more direct strategies would expand the accessible chemical space of biaryl-type NGs and accelerate materials discovery.

A direct C–H coupling would represent the most straightforward route to biaryl-type NGs. While transition-metal-catalyzed,[18,19] photoredox-catalyzed,[20,21] or hypervalent iodine[22,23]-mediated biaryl couplings of simpler arenes, such as benzene and naphthalene derivatives, are known, these methods tend to be less effective for π-extended PAHs, where multiple reactive sites and oxidative instability result in poor regioselectivity or even decomposition.[18,24,25] Classical BINOL synthesis elegantly exploits the hydroxyl group to direct coupling at the C1 position of 2-naphthol, yet analogous strategies have rarely succeeded in π-extended systems due to overoxidation of the biaryl product (Fig. 2a).[16,26–31] Despite recent advances in π-extended systems, the synthesis of axially chiral 3D NGs *via* Scholl-type C–H coupling remains a major challenge and has been only rarely achieved.[13,15]

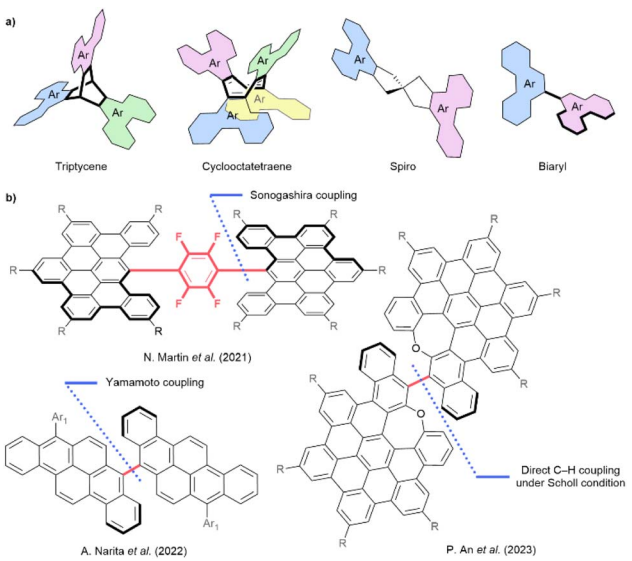

Fig. 1 (a) Representative core scaffolds of reported 3D NGs. Polycyclic aromatic hydrocarbon moiety (═Ar) is simplified and shown. (b) Reported axially chiral 3D NGs and their synthetic strategies. R = *tert*-butyl, Ar_1 = 2,4,6-trimethylphenyl.

[a]*Graduate School of Pharmaceutical Sciences, Kyoto University, Yoshida, Sakyo-ku, Kyoto 606–8501, Japan. E-mail: takasu.kiyosei.6r@kyoto-u.ac.jp*

[b]*Institute for Chemical Research, Kyoto University, Gokasho Uji-city, Kyoto 611-0011, Japan*

© 2026 The Author(s). Published by the Royal Society of Chemistry

Open Access Article. Published on 10 February 2026. Downloaded on 3/24/2026 4:28:19 PM.
This article is licensed under a Creative Commons Attribution-NonCommercial 3.0 Unported Licence.

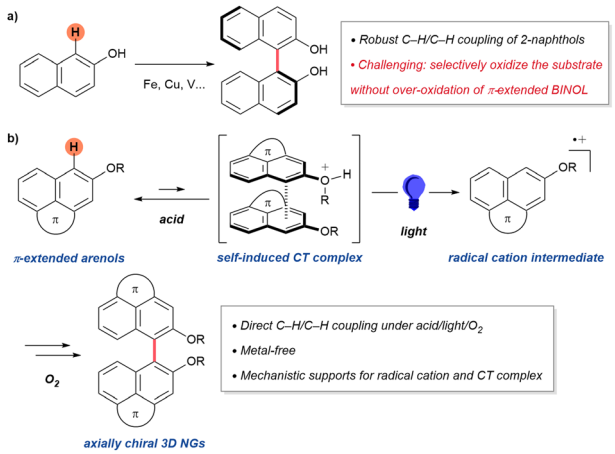

Fig. 2 (a) Classical approach to synthesize BINOL. (b) Metal-free C–H/C–H biaryl coupling of π-extended arenols enabled by self-induced CT complex under acid/light/O_2 condition (this work).

To overcome this limitation, we envisioned a photo-irradiated self-activation mechanism: an *in situ* transient protonated π-extended arenol with its neutral one generates a self-induced pseudo-homo charge transfer (CT) complex, which upon photoexcitation produces a radical cation competent for C–H coupling. Unlike the persistent hetero CT complexes between separate electron donors and acceptors reported by Sanford[32,33] and Kozlowski,[34,35] our system relies on intramolecular charge polarization within a single arenol scaffold. This design allows oxidative coupling of large, π-extended substrates while suppressing overoxidation through steric and electronic self-regulation. Specifically, because the targeted products are 3D NGs, their nonplanar geometry imposes substantial steric hindrance that prevents close π–π interaction between arenol units, making CT complexation less favorable. As a result, overoxidation of the resulting biaryl products, a common issue in π-extended systems, is mitigated. Herein, we report an acid, light and O_2 mediated C–H/C–H biaryl coupling, elucidate its mechanism, and disclose the properties of axially chiral 3D NGs.

Results and discussion

Optimization

During the course of our study on non-benzenoid PAHs,[36–38] we commenced our study with the oxidative biaryl coupling of dibenzo[*j*,*l*]fluoranthene **1a** as a model substrate, followed by optimization of the reaction conditions (Table 1). Following a comprehensive evaluation of reaction parameters, we found that 430 nm LEDs irradiation of a solution of **1a** in CH_2Cl_2/TFA (v/v = 9/1) under air for 6 h at 20 °C afforded the desired biaryl product **2a** in 90% yield (entry 1). Notably, **2a** was obtained as a single regioisomer, and this regioselectivity is supported by DFT calculations (see Fig. S26). No conversion was observed in the absence of TFA (entry 2), underscoring the crucial role of Brønsted acid in this transformation. Replacement of TFA ($pK_a = -0.3$) with weaker acid such as acetic acid (AcOH, $pK_a = +4.8$) resulted in full recovery of **1a** (entry 3). Conversely, the use of a stronger acid, methanesulfonic acid (MsOH, $pK_a = -2.6$) restored high efficiency, affording **2a** in 90% yield (entry 4). The reaction proved highly sensitive to the atmosphere: under N_2, the yield plummeted, indicating that O_2 serves as a terminal oxidant (entry 5). In the dark, performing the reaction led to only trace amounts of product (entry 6), confirming the indispensable role of photoirradiation. Taken together, these results indicate that the combination of Brønsted acid, O_2, and light is essential for this oxidative biaryl coupling reaction. Notably, applying known BINOL coupling conditions, such as $FeCl_3$ (entry 7) or DDQ (entry 8) as oxidants (representative examples; see Table S5), to **1a** led to negligible conversion or severe over-oxidation, resulting in poor mass balance.

Table 1 Optimization of reaction conditions[a]

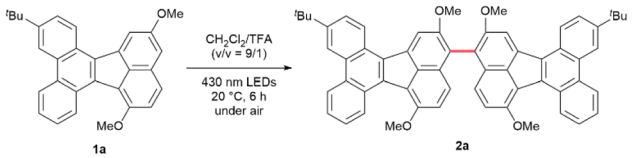

Entry	Deviation	Yields[b] (%) 2a	1a (recov.)
1	**None**	**90 (85)**	0
2	No TFA	0	86
3	AcOH instead of TFA	0	93
4	MsOH instead of TFA	90	0
5	N_2 instead of air	2	91
6	In dark	7	79
Known conditions			
7[c]	$FeCl_3$ in EtOH, reflux	(8)	(87)
8[d]	DDQ and TfOH in CH_2Cl_2, 0 °C	21	3

[a] Reaction conditions: **1a** (0.030 mmol) in CH_2Cl_2/TFA (v/v = 9/1, 0.030 M) at 20 °C for 6 h, irradiating with 430 nm LEDs. [b] Yields were determined by ^1H NMR using triphenylmethane as an internal standard. Isolated yield was shown in parentheses. [c] Reaction conditions: **1a** (0.050 mmol) and $FeCl_3$ (0.20 mmol) in EtOH (1.4 mL) at 95 °C (reflux) for 15 h. [d] Reaction conditions: **1a** (0.050 mmol), DDQ (0.10 mmol) and TfOH (0.30 mmol) in CH_2Cl_2 (5.0 mL) at 0 °C for 10 min.

Substrate scope

With the optimized reaction conditions in hand, we next investigated the substrate scope of fluoranthene derivatives **1** in dimerization reaction (Fig. 3). As a preliminary investigation, we evaluated the effect of varying the C1 substituent on a 5-methoxydibenzo[*j*,*l*]fluoranthene scaffold (**1a–1d**). Electron donating groups at C1 (**1a**, **1b**) and the unsubstituted parent substrate (**1c**) were well tolerated in this reaction, giving corresponding axially chiral 3D NGs **2a–2c** in high yield (85%, 99% and 75%, respectively). In contrast, introduction of an electron withdrawing group at C1 (**1d**) led to a markedly lower yield (28%), indicating that high electron density of an aromatic ring is essential for efficient dimerization. Next, we used 5-

Open Access Article. Published on 10 February 2026. Downloaded on 3/24/2026 4:28:19 PM.
This article is licensed under a Creative Commons Attribution-NonCommercial 3.0 Unported Licence.

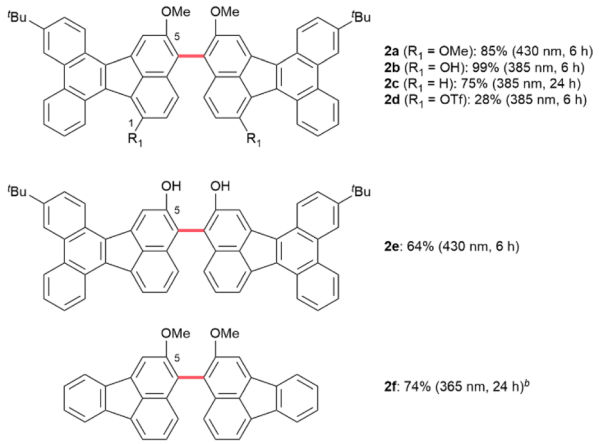

Fig. 3 Substrate scope for fluoranthene derivatives **1**[a]. [a]Reaction conditions: **1** (0.030 mmol) in CH_2Cl_2/TFA (v/v = 9/1, 0.030 M) at 20 °C. Isolated yields are shown. Wavelength of LEDs and reaction time are indicated in parentheses. [b]0.20 mmol of **1f** and MsOH instead of TFA were conducted.

hydroxydibenzo[*j*,*l*]fluoranthene (**1e**) as a substrate, and the dimerization proceeded in a moderate yield (64%). We attribute the slight decrease in yield compared to **1a–1c** to the instability of **1e**, which is prone to oxidation under air. Finally, 5-m-ethoxyfluoranthene (**1f**) afforded a high yield (74%) of **2f**, albeit that required replacement of TFA with MsOH.

Furthermore, to delineate the substrate scope beyond the fluoranthene scaffold, we investigated the dimerization reaction using other arenols (Fig. 4). Reaction parameters (irradiation wavelength, reaction temperature and time) were tailored to each substrate, and the addition of MS3A provided a modest increase in yield (see Table S6–S14). With 2-pyrenol (**3a**), the corresponding dimer **4a** was isolated in 82% yield and its structure was confirmed by X-ray crystallographic analysis. 9-Phenanthrenol (**3b**) and 2-anthracenol (**3c**) likewise furnished the corresponding dimers (76% and 48%, respectively). Notably, this dimerization reaction using **3b** can be performed on a 1.0 mmol scale without loss in efficiency (85%). In the naphthalene skeletons, 2-hydroxynaphthalene (**3d**) gave BINOL in 70% yield, whereas 2-methoxynaphthalene (**3e**) afforded only 12% yield with 70% recovery of **3e**; this difference is consistent with the lower propensity of **3e** to form the CT complex under these conditions (see Fig. S14 and S18). 1,4-Bis(2-naphthoxy) butane (**3f**) did not deliver the intramolecular product **4f**, likely because the tether restricted conformational freedom and disfavored formation of CT complex. In addition, 2,3- and 2,7-dihydroxynaphthalene (**3g**, **3h**) reacted smoothly, and 2,6-dihydroxynaphthalene (**3i**) furnished **4i** in high yield (72%). Using 2-hydroxy-6-methoxynaphthalene (**3j**) gave two regioisomers, **4j** (C1–C1′) and **4j′** (C1–C5′), in a 7 : 1 ratio (62% yield). Consistent with the result for **3e**, 2,6-dimethoxynaphthalene (**3k**) afforded a lower yield (25%) of dimer **4k**. Collectively, these results showed that our dimerization protocol was effective not only for the fluoranthene scaffold but also for several other PAHs.

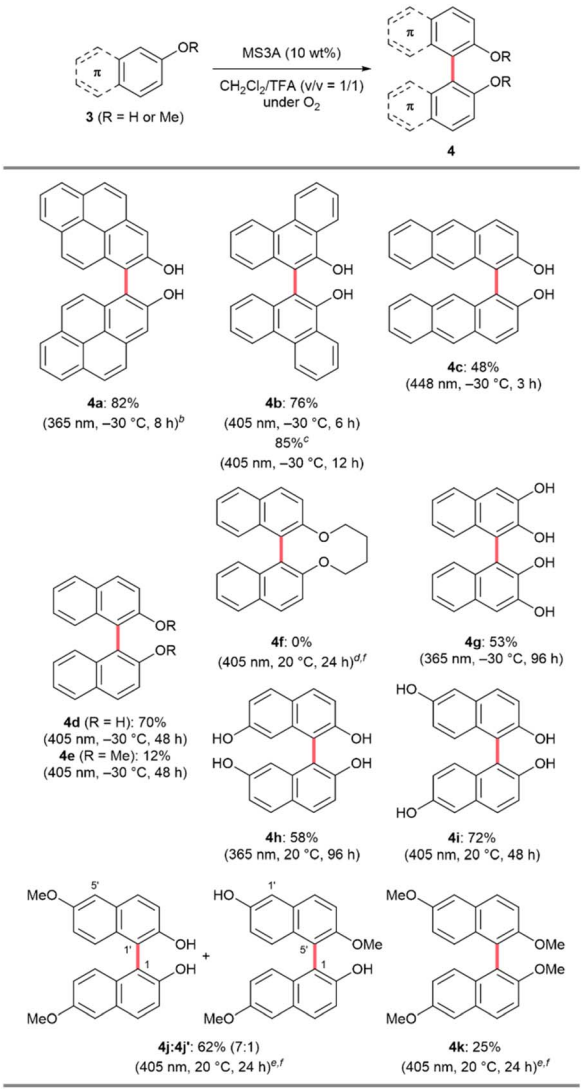

Fig. 4 Substrate scope. [a]Reaction conditions: **3** (0.40 mmol) and MS3A (10 wt%) in CH_2Cl_2/TFA (v/v = 1/1, 0.10 M). Wavelength of LEDs, reaction temperature and time are indicated in parentheses. Isolated yields are shown. [b]0.20 mmol of **3a**. [c]On 1.0 mmol scale. [d]0.060 mmol of **3f** in CH_2Cl_2/TFA (v/v = 9/1, 0.015 M). [e]0.12 mmol of substrate in CH_2Cl_2/TFA (v/v = 9/1, 0.030 M). [f]Without MS3A.

Mechanistic studies

To gain insight into the reaction mechanism, we first recorded the UV-vis absorption spectra of **1a** (Fig. 5a). In CH_2Cl_2, no significant absorption was observed above 550 nm. However, in CH_2Cl_2/TFA (v/v = 9/1), its UV-vis spectrum displayed a new broad absorption band with a maximum at *ca.* 640 nm and a tail extending into the near-infrared (NIR) region. This spectral change suggests the formation of a new species under acidic conditions. The absorption at 640 nm was further enhanced upon photoirradiation. To further investigate the reaction mechanism, we conducted the biaryl coupling reaction in the presence of TEMPO (5.0 eq.), a well-known radical scavenger (Fig. 5b). In this case, the reaction gave a complex mixture, suggesting the involvement of radical intermediates. To further

 © 2026 The Author(s). Published by the Royal Society of Chemistry

Open Access Article. Published on 10 February 2026. Downloaded on 3/24/2026 4:28:19 PM.
This article is licensed under a Creative Commons Attribution-NonCommercial 3.0 Unported Licence.

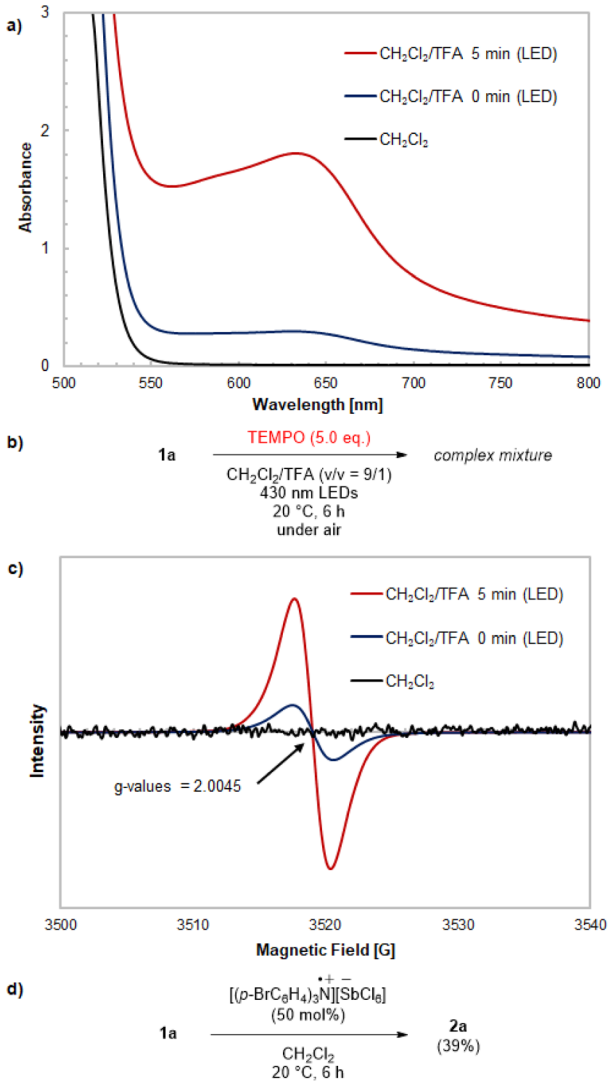

Fig. 5 Mechanistic studies. (a) UV-vis absorption and (c) ESR spectra of **1a** (30 mM). Black line: in CH_2Cl_2, blue line: in CH_2Cl_2/TFA (v/v = 9/1), red line: in CH_2Cl_2/TFA (v/v = 9/1) upon irradiation with 430 nm LEDs for 5 min. (b) Biaryl coupling with TEMPO as a radical scavenger. (d) Biaryl coupling with Magic Blue as a single electron oxidant.

support the formation of radical species, ESR spectroscopy was carried out (Fig. 5c). While no ESR signal was observed in CH_2Cl_2 alone, an ESR signal (g = 2.0045) appeared in CH_2Cl_2/TFA (v/v = 9/1), consistent with the formation of a typical radical species.[39,40] Moreover, photoirradiation led to a further increase in ESR signal intensity, indicating that light promotes the generation of the radical species. Finally, we employed tris(4-bromophenyl)ammoniumyl hexachloroantimonate (Magic Blue) as an external single electron oxidant without TFA and light irradiation (Fig. 5d). As a result, the biaryl coupling reaction proceeded smoothly, indicating that a radical cation intermediate $\mathbf{1a}^{\bullet+}$ is involved in the reaction pathway. UV-vis titration of **1a** with Magic Blue reproduced the *ca.* 640 nm band and TD-DFT calculations assign this transition to $\mathbf{1a}^{\bullet+}$ (see Fig. S12, S25 and Table S28).

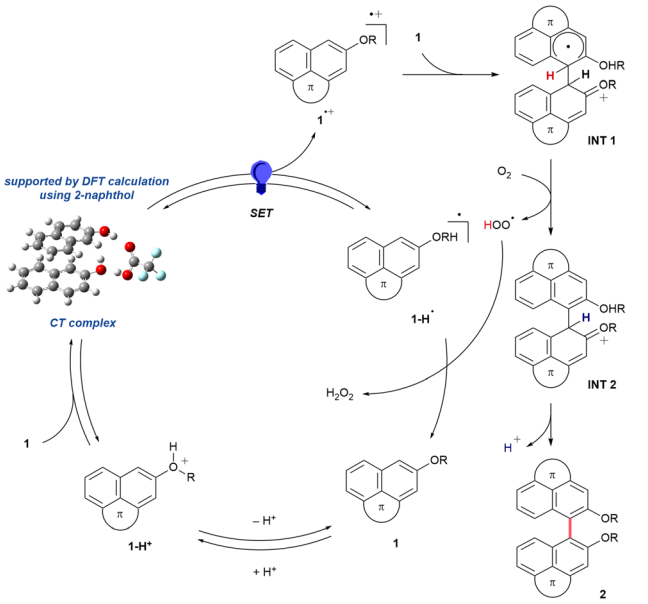

Scheme 1 Proposed mechanism. Fluoranthene **1** is shown in a simplified form for clarity (R = Me or H).

Proposed mechanism

Based on our observations, we propose the reaction mechanism depicted in Scheme 1. A self-induced pseudo-homo CT complex is first formed between neutral fluoranthene **1** and its protonated counterpart (**1-H**$^+$). Geometry optimization using 2-naphthol as a simplified model supports the feasibility of such an association, and subsequent natural transition orbital (NTO) analysis[41] indicates that photoexcitation promotes intramolecular charge transfer leading to a radical cation species (see Fig. S17). The radical cation ($\mathbf{1}^{\bullet+}$) subsequently undergoes coupling with **1** to form intermediate **INT 1**.[42,43] Then, O_2 formally abstracts a hydrogen atom from **INT 1** to give **INT 2**, while the resulting HOO$^\bullet$ abstracts another hydrogen atom from **1-H**$^\bullet$, thereby generating H_2O_2 and simultaneously regenerating **1**.[32,34,35] Finally, deprotonation of **INT 2** furnishes the axially chiral 3D NG **2**.

Physical properties

To further investigate the chiroptical properties of the coupling products, we subjected *rac*-**2a** to chiral HPLC, which clearly separated the two enantiomers ((+)-**2a** and (−)-**2a**) that exhibited mirror-image CD spectra (Fig. 6a). Comparison of the experimental CD spectra with TD-DFT calculations enabled assignment of (−)-**2a** as the R enantiomer. Theoretical calculations revealed a high racemization barrier of the model structure ($\Delta G^{\ddagger}_{calc}$ = 36.5 kcal mol^{-1}), which is comparable to that of typical BINOL derivatives.[44] This theoretically estimated racemization barrier is in good agreement with the experimentally estimated one ($\Delta G^{\ddagger}_{exp}$ = 36.9 kcal mol^{-1}), supporting the calculated racemization mechanism (see Fig. S27 and S28). Finally, the photophysical properties of fluoranthene **1a** and axially chiral 3D NG **2a** were compared (Fig. 6b). In the UV-vis

Open Access Article. Published on 10 February 2026. Downloaded on 3/24/2026 4:28:19 PM.
This article is licensed under a Creative Commons Attribution-NonCommercial 3.0 Unported Licence.

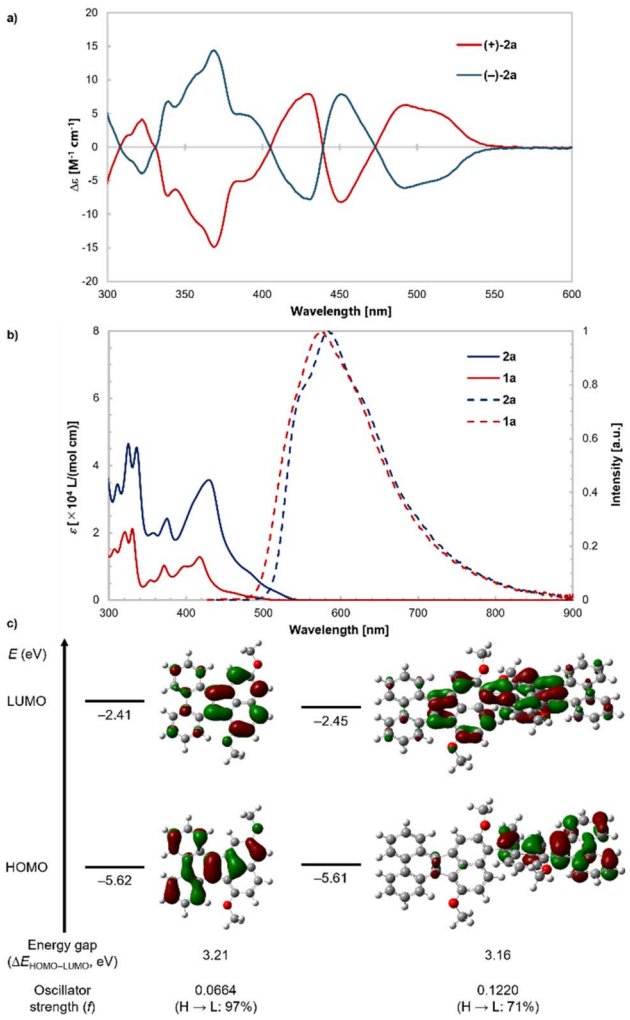

Fig. 6 (a) CD spectra of **2a** in $CHCl_3$ at 298 K. (b) UV-vis absorption (solid line) and fluorescence (dashed line) spectra of **1a** and **2a** in CH_2Cl_2 at 298 K. (c) Calculated frontier molecular orbitals, energy levels ($\Delta E_{HOMO-LUMO}$) and oscillator strengths (f) of **1a′** and **2a′** (^{t}Bu groups are omitted) at the B3LYP/6-31+G (d,p)-CPCM(CH_2Cl_2) level of theory. The contribution of the HOMO to LUMO transition is shown in parentheses below the f value.

absorption spectrum, **1a** displayed pronounced absorption bands at 418 nm ($\varepsilon = 1.28 \times 10^4$ L mol^{-1} cm^{-1}) and a broad feature spanning 430–500 nm. **2a** showed a closely related profile to **1a**, characterized by an intense band at 430 nm ($\varepsilon = 3.57 \times 10^4$ L mol^{-1} cm^{-1}) together with a broad absorption in the 450–520 nm region. To gain further insight into this feature, TD-DFT calculations were performed at the B3LYP/6-31+G(d,p)-CPCM(CH_2Cl_2) level of theory, employing model substrates **1a′** and **2a′** with ^{t}Bu groups omitted (Fig. 6c). The calculated HOMO and LUMO of **1a′** were similar to those of typical dibenzo[*j*,*l*] fluoranthenes.[38] The HOMO of **2a′** was localized on one fluoranthene unit, while the LUMO was delocalized over both units. The HOMO–LUMO energy gaps ($\Delta E_{HOMO-LUMO}$, eV) and the oscillator strengths (f) are in good agreement with observed trends in UV-vis absorption. In the fluorescence spectrum, **2a** exhibited a slightly red-shifted emission maximum ($\lambda_{em} = 584$ nm) compared to **1a** ($\lambda_{em} = 575$ nm). The fluorescence quantum yield (Φ) of **2a** (2.6%) was higher than that of **1a** (1.7%). Because both **1a** and **2a** are intrinsically rigid and undergo little structural change upon excitation, the enhanced fluorescence efficiency of **2a** can be ascribed to its more allowed S_0–S_1 transition, as reflected by the larger oscillator strength obtained from TD-DFT calculations.

Conclusions

In summary, we have developed a Brønsted acid, light, and O_2 driven protocol for oxidative C–H/C–H biaryl coupling from π-extended arenols. This method provides direct access to axially chiral 3D NGs, including those derived from non-benzenoid fluoranthene scaffolds. The scope of this reaction extends to a variety of arenols beyond fluoranthenes, underscoring the generality of this approach. Mechanistic studies revealed that the transformation proceeds *via* radical cation intermediates, while computational analysis predicted the formation of a self-induced pseudo-homo CT complex under acidic conditions, rationalizing the observed reactivity. This metal-free and direct C–H coupling provides a general strategy for designing π-extended chiral NGs with tailored photophysical and chiroptical properties.

Author contributions

K. K. discovered the reaction and performed the experiments, measurements and calculations. K. T. directed the project with A. K., Y. K. and H. T. K. T. -K. helped to perform ESR experiment and discussed. K. K. prepared the manuscript with input from all authors.

Conflicts of interest

There are no conflicts to declare.

Data availability

CCDC 2498496, 2498947, 2498498, 2498499, 2498500, 2498501, and 2498502 (**1a**, **1b**, **1d**, **2a**, **2d**, **2f** and **4a**) contain the supplementary crystallographic data for this paper.[45a–g]

The authors confirm that the data supporting the findings of this study are available within the article and its supplementary information (SI). Supplementary information is available. See DOI: https://doi.org/10.1039/d5sc09144f.

Acknowledgements

This study was supported by a JSPS KAKENHI (23H02604; KT), MEXT KAKENHI (21H05211; KT) in Digi-TOS, BINDS from AMED (22ama121034j0001; KT), and JST SPRING (JPMJSP2110; KK).

Notes and references

1 V. Kumar, J. L. Páez, S. Míguez-Lago, J. M. Cuerva, C. M. Cruz and A. G. Campaña, *Chem. Soc. Rev.*, 2025, **54**, 4922–4947.

 © 2026 The Author(s). Published by the Royal Society of Chemistry

Open Access Article. Published on 10 February 2026. Downloaded on 3/24/2026 4:28:19 PM.
This article is licensed under a Creative Commons Attribution-NonCommercial 3.0 Unported Licence.

2 C. Zhang, Y. Liu, X.-Q. Xiong, L.-H. Peng, L. Gan, C.-F. Chen and H.-B. Xu, *Org. Lett.*, 2012, **14**, 5912–5915.
3 B.-L. Hu, C. An, M. Wagner, G. Ivanova, A. Ivanova and M. Baumgarten, *J. Am. Chem. Soc.*, 2019, **141**, 5130–5134.
4 D. P. Sumy, N. J. Dodge, C. M. Harrison, A. D. Finke and A. C. Whalley, *Chem. Eur J.*, 2016, **22**, 4709–4712.
5 R. Kumar, P. J. Chmielewski, T. Lis, D. Volkmer and M. Stępień, *Angew. Chem., Int. Ed.*, 2022, **61**, e202207486.
6 J. Urieta-Mora, M. Krug, W. Alex, J. Perles, I. Fernández, A. Molina-Ontoria, D. M. Guldi and N. Martín, *J. Am. Chem. Soc.*, 2020, **142**, 4162–4172.
7 P. Liu, H.-H. Lv, R. Xue, X.-Y. Tang, X.-Y. Chen, L. Qi and X.-Y. Wang, *Org. Mater.*, 2024, **6**, 40–44.
8 P. Izquierdo-García, J. M. Fernández-García, J. Perles, I. Fernández and N. Martín, *Angew. Chem., Int. Ed.*, 2023, **62**, e202215655.
9 J. Lión-Villar, J. M. Fernández-García, S. M. Rivero, J. Perles, S. Wu, D. Aranda, J. Wu, S. Seki, J. Casado and N. Martín, *Nat. Chem.*, 2025, **17**, 1099–1106.
10 K. K. Laali, T. Okazaki and S. E. Galembeck, *J. Chem. Soc., Perkin Trans. 2*, 2002, 621–629.
11 P. Izquierdo-García, J. M. Fernández-García, I. Fernández, J. Perles and N. Martín, *J. Am. Chem. Soc.*, 2021, **143**, 11864–11870.
12 X. Xu, S. Gunasekaran, S. Renken, L. Ripani, D. Schollmeyer, W. Kim, M. Marcaccio, A. Musser and A. Narita, *Adv. Sci.*, 2022, **9**, 2200004.
13 S. Li, R. Li, Y.-K. Zhang, S. Wang, B. Ma, B. Zhang and P. An, *Chem. Sci.*, 2023, **14**, 3286–3292.
14 L. Qin, J. Xie, B. Wu, H. Hong, S. Yang, Z. Ma, C. Li, G. Zhang, X.-S. Zhang, K. Liu and D. Zhang, *J. Am. Chem. Soc.*, 2024, **146**, 12206–12214.
15 X. Zhang, H. Ma, Q. Yin, F. Bai, Y. Hashikawa and Chaolumen, *Org. Lett.*, 2025, **27**, 8969–8973.
16 K. Nakano, Y. Hidehira, K. Takahashi, T. Hiyama and K. Nozaki, *Angew. Chem., Int. Ed.*, 2005, **44**, 7136–7138.
17 M. Sako, Y. Takeuchi, T. Tsujihara, J. Kodera, T. Kawano, S. Takizawa and H. Sasai, *J. Am. Chem. Soc.*, 2016, **138**, 11481–11484.
18 Y. Yang, J. Lan and J. You, *Chem. Rev.*, 2017, **117**, 8787–8863.
19 J. Vercammen, M. Bocus, S. Neale, A. Bugaev, P. Tomkins, J. Hajek, S. V. Minnebruggen, A. Soldatov, A. Krajnc, G. Mali, V. V. Speybroeck and D. E. D. Vos, *Nat. Catal.*, 2020, **3**, 1002–1009.
20 M. H. Aukland, M. Šiaučiulis, A. West, G. J. P. Perry and D. J. Procter, *Nat. Catal.*, 2020, **3**, 163–169.
21 X. Wang, X. Xun, H. Song, Y. Liu and Q. Wang, *Org. Lett.*, 2022, **24**, 4580–4585.
22 T. Takada, M. Arisawa, M. Gyoten, R. Hamada, H. Tohma and Y. Kita, *J. Org. Chem.*, 1998, **63**, 7698–7706.
23 T. Dohi, K. Morimoto, Y. Kiyono, A. Maruyama, H. Tohma and Y. Kita, *Chem. Commun.*, 2005, 2930–2932.
24 A. Kumar, H. Sasai and S. Takizawa, *Acc. Chem. Res.*, 2022, **55**, 2949–2965.
25 J. Wu, Y. Koga, G. Hong, M. E. Rotella and M. C. Kozlowski, *J. Am. Chem. Soc.*, 2025, **147**, 34089–34100.
26 J. M. Brunel, *Chem. Rev.*, 2005, **105**, 857–897.
27 J.-M. Tian, A.-F. Wang, J.-S. Yang, X.-J. Zhao, Y.-Q. Tu, S.-Y. Zhang and Z.-M. Chen, *Angew. Chem., Int. Ed.*, 2019, **58**, 11023–11027.
28 S.-H. Wang, S.-Q. Wei, Y. Zhang, X.-M. Zhang, S.-Y. Zhang, K.-L. Dai, Y.-Q. Tu, K. Lu and T.-M. Ding, *Nat. Commun.*, 2024, **15**, 4591.
29 S. Zhang, Y. Wang, Z. Song, K. Nakajima and T. Takahashi, *Chem. Lett.*, 2013, **42**, 697–699.
30 S. Takizawa, J. Kodera, Y. Yoshida, M. Sako, S. Breukers, D. Enders and H. Sasai, *Tetrahedron*, 2014, **70**, 1786–1793.
31 K. Hassan, K. Yamashita, K. Hirabayashi, T. Shimizu, K. Nakabayashi, Y. Imai, T. Matsumoto, A. Yamano and K. Sugiura, *Chem. Lett.*, 2015, **44**, 1607–1609.
32 M. R. Lasky, T. K. Salvador, S. Mukhopadhyay, M. S. Remy, T. P. Vaid and M. S. Sanford, *Angew. Chem., Int. Ed.*, 2022, **61**, e202208741.
33 D. S. Brandes, M. R. Lasky, A. V. R. D. Lisboa, E.-C. Liu, M. S. Remy and M. S. Sanford, *Org. Lett.*, 2025, **27**, 10011–10015.
34 M. C. Carson, C. R. Liu, Y. Liu and M. C. Kozlowski, *ACS Catal.*, 2024, **14**, 12173–12180.
35 M. C. Carson, C. R. Liu and M. C. Kozlowski, *J. Org. Chem.*, 2024, **89**, 3419–3429.
36 N. Ogawa, Y. Yamaoka, K. Yamada and K. Takasu, *Org. Lett.*, 2017, **19**, 3327–3330.
37 N. Ogawa, Y. Yamaoka, H. Takikawa, K. Yamada and K. Takasu, *J. Am. Chem. Soc.*, 2020, **142**, 13322–13327.
38 K. Kurokawa, N. Ogawa, Y. Kuroda, Y. Yamaoka, H. Takikawa, K. Tsubaki and K. Takasu, *Org. Biomol. Chem.*, 2024, **22**, 5306–5313.
39 Y. Kita, H. Tohma, K. Hatanaka, T. Takada, S. Fujita, S. Mitoh, H. Sakurai and S. Oka, *J. Am. Chem. Soc.*, 1994, **116**, 3684–3691.
40 A. M. Genaev, L. N. Shchegoleva, G. E. Salnikov, A. V. Shernyukov, L. A. Shundrin, I. K. Shundrina, Z. Zhu and K. Y. Koltunov, *J. Org. Chem.*, 2019, **84**, 7238–7243.
41 R. L. Martin, *J. Chem. Phys.*, 2003, **118**, 4775–4777.
42 H. Tohma, M. Iwata, T. Maegawa and Y. Kita, *Tetrahedron Lett.*, 2002, **43**, 9241–9244.
43 H. Choi, S.-E. Suh and H. Kang, *Adv. Synth. Catal.*, 2024, **366**, 4347–4384.
44 L. Meca, D. Řeha and Z. Havlas, *J. Org. Chem.*, 2003, **68**, 5677–5680.
45 (*a*) CCDC 2498496: Experimental Crystal Structure Determination, 2026, DOI: 10.5517/ccdc.csd.cc2pvwn3; (*b*) CCDC 2498497: Experimental Crystal Structure Determination, 2026, DOI: 10.5517/ccdc.csd.cc2pvwp4; (*c*) CCDC 2498498: Experimental Crystal Structure Determination, 2026, DOI: 10.5517/ccdc.csd.cc2pvwq5; (*d*) CCDC 2498499: Experimental Crystal Structure Determination, 2026, DOI: 10.5517/ccdc.csd.cc2pvwr6; (*e*) CCDC 2498500: Experimental Crystal Structure Determination, 2026, DOI: 10.5517/ccdc.csd.cc2pvws7; (*f*) CCDC 2498501: Experimental Crystal Structure Determination, 2026, DOI: 10.5517/ccdc.csd.cc2pvwt8; (*g*) CCDC 2498502: Experimental Crystal Structure Determination, 2026, DOI: 10.5517/ccdc.csd.cc2pvwv9.